Molecular Level Synthesis of $InFeO_3$ and $InFeO_3/Fe_2O_3$ Nanocomposites

Vanessa Nahrstedt[1], *Daniel Stadler*[1], *Thomas Fischer*[1], *Tomáš Duchoň*[2], *David N. Mueller*[2], *Claus M. Schneider*[2], *Sanjay Mathur**[1]

[1]Institute of Inorganic Chemistry, University of Cologne, Greinstr. 6, 50939 Cologne, Germany

[2]PGI-6, Research Centre Juelich GmbH, Leo-Brandt-Str., 52428 Juelich, Germany

KEYWORDS metal alkoxides, indium ferrite, single-source precursor, magnetism

ABSTRACT. New heterometallic In-Fe alkoxides $[InFe(O^tBu)_4(PyTFP)_2]$ (**1**), $[InFe_2(O^{neo}Pen)_9(Py)]$ (**2**) and $[InFe_3(O^{neo}Pen)_{12}]$ (**3**) were synthesized and structurally characterized. The arrangement of metal centers in mixed-metal framework was governed by the In:Fe ratio and the coordination preferences of Fe(III) and In(III) centers to be in tetrahedral and octahedral environments, respectively. **3** displayed a star-shaped so-called "Mitsubishi" motif with central In atom coordinated with three tetrahedral $\{Fe(O^{neo}Pen)_4\}^-$ anionic units. The deterministic structural influence of larger In atom was evident **1** and **2** that displayed the coordination of neutral co-ligands to achieve the desired coordination number. Thermal decomposition studies of compounds **1**-**3** under inert conditions with subsequent powder diffraction studies revealed the formation of Fe_2O_3 and In_2O_3 in case of **3** and **2,** whereas **1** intriguingly produced elemental In and Fe. In contrary, thermal decomposition of **1**-**3** under ambient conditions produced a ternary oxide, $InFeO_3$, with additional Fe_2O_3 present as a secondary phase in different stoichiometric ratio predetermined through In:Fe ratio in **2** and **3**.

The intimate mixing of different phases in $InFeO_3/Fe_2O_3$ nanocomposites was confirmed by transmission electron microscopy of solid residues obtained after the decomposition of **1** and **2**. The pure $InFeO_3$ particles demonstrated ferromagnetic anomalies around 170 K as determined by temperature-dependent field-cooled and zero-field-cooled magnetization experiments. A first order magnetic transition with an increase in the ZFC measurements was explained by temperature induced reduction of the Fe-Fe distance and the corresponding increase in super-exchange.

INTRODUCTION. Heterometallic alkoxides are intrinsically efficient precursors to mixed-metal oxides due to pre-formed heterometallic bridges connected through alkoxide oxygen (–M–(O)R–M’–) that generally allows their conversion to desired oxide ceramics without lengthy heat treatments since the formation of solid-state phases is not only driven by Fickian diffusion. Selective conversion of a large number of metal alkoxides to ternary ceramics and composites has been demonstrated to verify the role precursor chemistry plays in the synthesis of phase pure material[1,2,11–20,3,21–24,4–10] Formation of nano-scaled composites from molecular sources allows to tailor the material properties not possible by conventional synthesis methods, which generally lead to elemental segregation and phase separation. The sol-gel processing and gas phase depositions of monometallic metal alkoxides as single-source precursors are comprehensively studied, however mixed-metal compositions are relatively less investigated[4,7–9,11,12,15,25–45] Despite the potential advantages of chemical processing, the major constraint in the application of heterometallic alkoxides is related to their limited synthetic access and dearth of structural data on metal alkoxide frameworks.

Among binary oxides, ternary ferrites of general formula $MFeO_3$ (M = In, Y, Eu-Lu) are of fundamental interest, due to their physical and structural properties.[46,47] Recently, thin films of $InFeO_3$ (E_g = 2.5 eV), prepared *via* pulsed laser deposition, were considered as photoelectrodes for water-splitting reactions by visible and ultraviolet light[48]. In addition, the $LiNbO_3$-type of $InFeO_3$ is a room-temperature polar magnet that shows the functional properties of small tolerance-factor perovskites and is of fundamental interest due to canted G-type antiferromagnetic ordering of Fe^{3+} moments.[49–51] In the realm of mixed-metal iron-indium oxides, the antiferromagnet $InFe_2O_4$ is isostructural to $LuFe_2O_4$, which shows electrical polarization[52], and charge as well as magnetic ordering phenomena between 230 and 250 K, whereas $(In_{1-x}Fe_x)_2O_3$ phases show ferromagnetism at room temperature.[53,54] We report here, the synthesis and characterization of a new series of mixed metal alkoxide precursors

[InFe(O^{t}Bu)$_4$(PyTFP)$_2$] (**1**), [InFe$_2$(O^{neo}Pen)$_9$(Py)] (**2**) and [InFe$_3$(O^{neo}Pen)$_{12}$] (**3**) as well as their transformation into InFeO$_3$ for **1** and InFeO$_3$/Fe$_2$O$_3$ composites for **2** and **3**.

RESULTS AND DISCUSSION. The new series of mixed-metal alkoxides **1**-**3** were obtained by *in-situ* alcoholysis of [In{N(SiMe$_3$)$_2$}$_3$] in the presence of iron(III) *tert*-butoxide ([Fe(O^{t}Bu)$_3$]$_2$) and pyridine for **1** as well as the chelating anionic ligand HPyTFP in case of **2** (Figure 1). The molecular structures of **1**-**3** were confirmed by single crystal X-ray diffraction analysis (Figure 2).

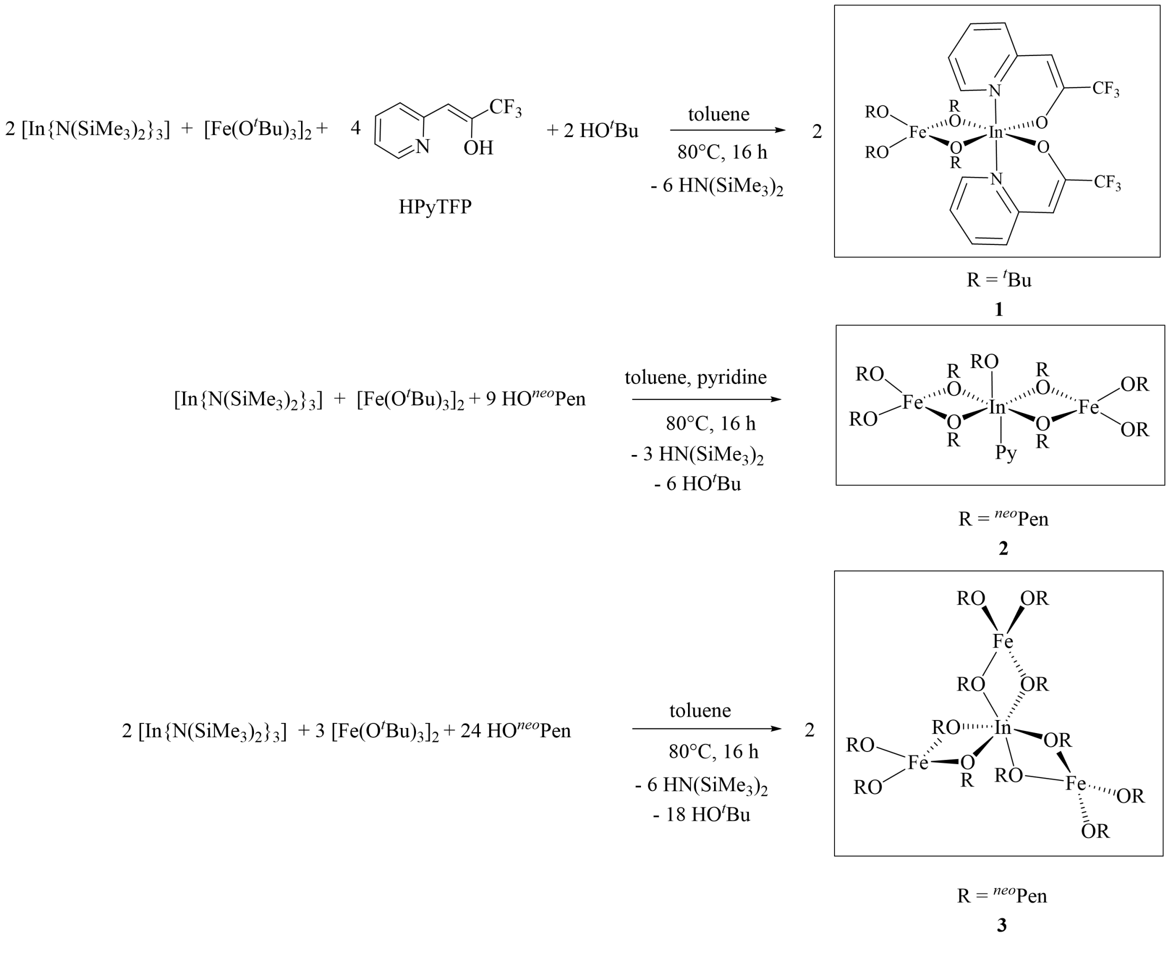

Figure 1: Schematic synthesis of heterometallic alkoxides [InFe(O^{t}Bu)$_4$(PyTFP)$_2$] (**1**), [InFe$_2$(O^{neo}Pen)$_9$(Py)] (**2**) and [InFe$_3$(O^{neo}Pen)$_{12}$] (**3**).

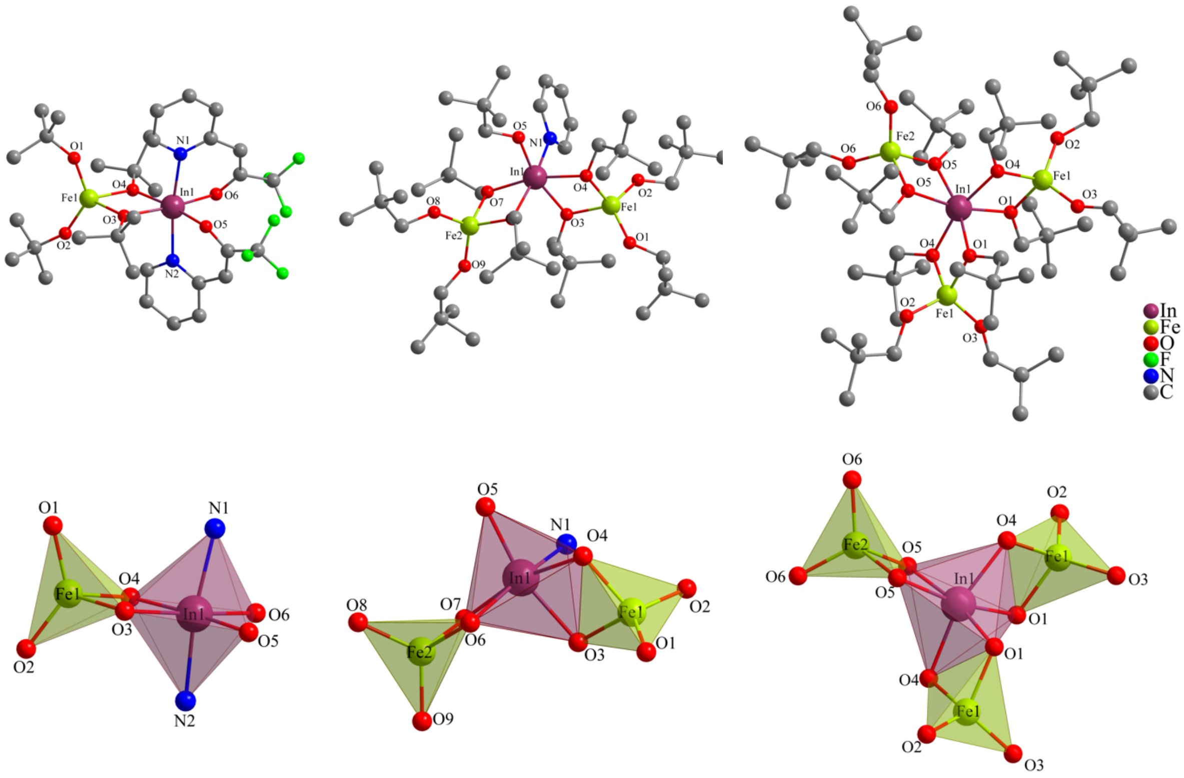

$[InFe(O^tBu)_4(PyTFP)_2]$ **1** $[InFe_2(Py)(O^{neo}Pen)_9]$ **2** $[InFe_3(O^{neo}Pen)_{12}]$ **3**

Figure 2: Molecular structures of $[InFe(O^tBu)_4(PyTFP)_2]$ (**1**), $[InFe_2(O^{neo}Pen)_9(Py)]$ (**2**) and $[InFe_3(O^{neo}Pen)_{12}]$ (**3**) with different indium iron ratios as well as the coordination polyhedral of indium and iron, hydrogen atoms are omitted for clarity.

The molecular structures of **1**-**3** showed iron in a four-fold coordination of oxygen atoms formed by two terminal and two μ_2-bridging alkoxo ligands. Irrespective of the metal ratio (1:1, 1:2, 1:3), $\{Fe(OR)_4\}^-$ units (R = ^{neo}Pen (**2**, **3**), ^{t}Bu (**1**)) coordinate to the indium center in a bidentate fashion in all the three compounds. $[InFe_3(O^{neo}Pen)_{12}]$ (**3**) with In:Fe stoichiometry of 1:3 was found to consistently produce the "Mitsubishi" motif with central indium atom, coordinated by three bidentate $\{Fe(O^{neo}Pen)_4\}^-$ units. The compounds based on In:Fe ratio of 1:1 and 1:2 displayed in **1** and **2**, respectively highlighted the necessity of the coordination of both neutral or anionic co-ligands to form stable frameworks. $[InFe_2(O^{neo}Pen)_9(Py)]$ **2** displayed a linear arrangement of indium and iron centers with Fe present in characteristic tetrahedral coordination. The octahedral coordination preferred by indium atoms is achieved by a neutral pyridine ligand in [$InFe_2(O^{neo}Pen)_9(Py)$] (**2**) to ensure the preferred octahedral environment by larger In(III) (r(Fe^{3+}, *high spin*) = 65 pm and r(In^{3+}) = 80 pm).[55] Attempts directed to obtain 'donor-free' indium-iron complexes with 1:1 ratio were not successful, possibly due to the structural preferences observed in **2** and **3**. The incorporation of the anionic ligand HPyTFP, which has been used for stabilizing a large number of metals through its bidentate chelation, was found to increase the stability of the heterometallic framework based on 1:1 ratio between In and Fe that resulted in the formation of **1**.[32,56–63] The chelating ligand is coordinated to the indium metal center due to the larger ionic radius of indium (r(Fe^{3+}, *high spin*) = 65 pm and r(In^{3+}) = 80 pm).[55] However, the use of chelating ligands in the construction of heterometallic alkoxides represent a delicate interplay between the driving force for the formation of mixed metal assemblies and the stabilization of monometallic species. For example, an increased amount of PyTFP supports the formation of homometallic [$Fe(O^tBu)(PyTFP)_2$], which was not observed in the present study.

The suitability of **1**-**3** in the formation of In-Fe-O-ceramics was evaluated by thermogravimetric studies (Figure 3) for which the samples were gradually heated up to 600 °C under dry nitrogen atmosphere. The thermogravimetric measurements of **2** and **3** revealed multi-step decomposition in each case that can be ascribed to the sequential decomposition of ligands of different chemical strengths (alkoxide vs. alkenolate) present on different metal centers (In and Fe) to finally produce In_2O_3/Fe_2O_3-composites, which were analysed by powder XRD studies (Figure 3). The deviation of observed (**2**: $\Delta m(exp) = 70\%$, **3**: $\Delta m(exp) = 69\%$) and calculated mass loss (**2**: $\Delta m(calc) = 60\%$, **3**: $\Delta m(calc) = 67\%$) regarding the formation of In_2O_3/Fe_2O_3 composite can be attributed to partial hydrolysis of the heterometallic alkoxides during the transfer of the samples from the flasks to the alumina crucibles used in TG/DTA analyses. In contrast, thermogravimetric decomposition of the heterometallic alkoxide with 1:1 metal ratio (**1**) leading to the formation of In(0) and Fe(0) with a mass loss of 58%, which might be due to the reduction of metal centres by the ligands. The redox-activity of the heteroarylalkenolate ligands was observed for several metals before, e.g., cobalt and tin.[61,64] Regarding monometallic cobalt precursors $[Co^{II}(PyTFP)_2(DMAP)]$ (DMAP = 4-dimethylaminopyridin) and $[Co^{III}(PyTFP)_3]$, the PyTFP ligand caused not only the oxidation of the metal center (Co^{II} to Co^{III}), but also the reduction of Co^{III} to Co^{II} during gas phase deposition to synthesize Co_3O_4.

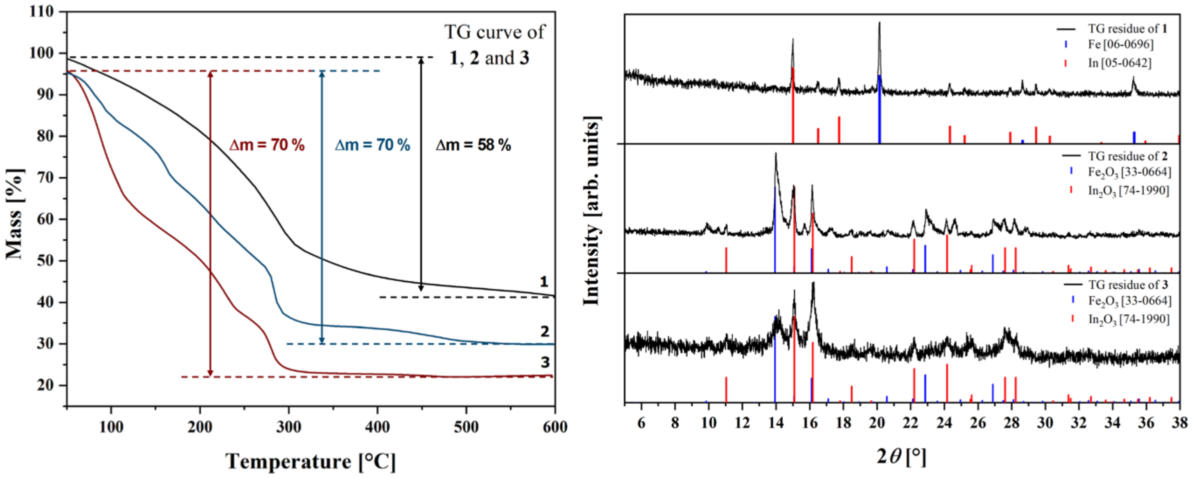

Figure 3: Thermogravimetry measurements of **1**-**3** upto 600 °C under N_2-atmosphere (left) and powder XRD of the residue after the measurements with literature data for Fe_2O_3 [33-0664], Fe [06-0696] in blue and In_2O_3 [74-1990], In [05-0642] in red (right).

In contrary to the chemical composition of the residual solids obtained upon performing the thermal decomposition under inert conditions, heating **1**-**3** in air at 1000 °C for 16 h with a heating rate of 300 °C/h produced ternary $InFeO_3$ (**1**), which was proven by XRD measurements (Figure 4). The additional α-Fe_2O_3 phase was formed in **2** and **3** due to an excess amount of iron present in $[InFe_2(O^{neo}Pen)_9(Py)]$ (**2**) and $[InFe_3(O^{neo}Pen)_{12}]$ (**3**). In case of **1**, low intensity peaks were observed around 23.2, 23.5, 16.4 and 16.5°, which couldn't be assigned to any expected phase of iron or indium oxides or their mixtures. Also, the formation of metal carbides can be ruled out based on the differential peak analysis with the powder diffraction files available in the databank.

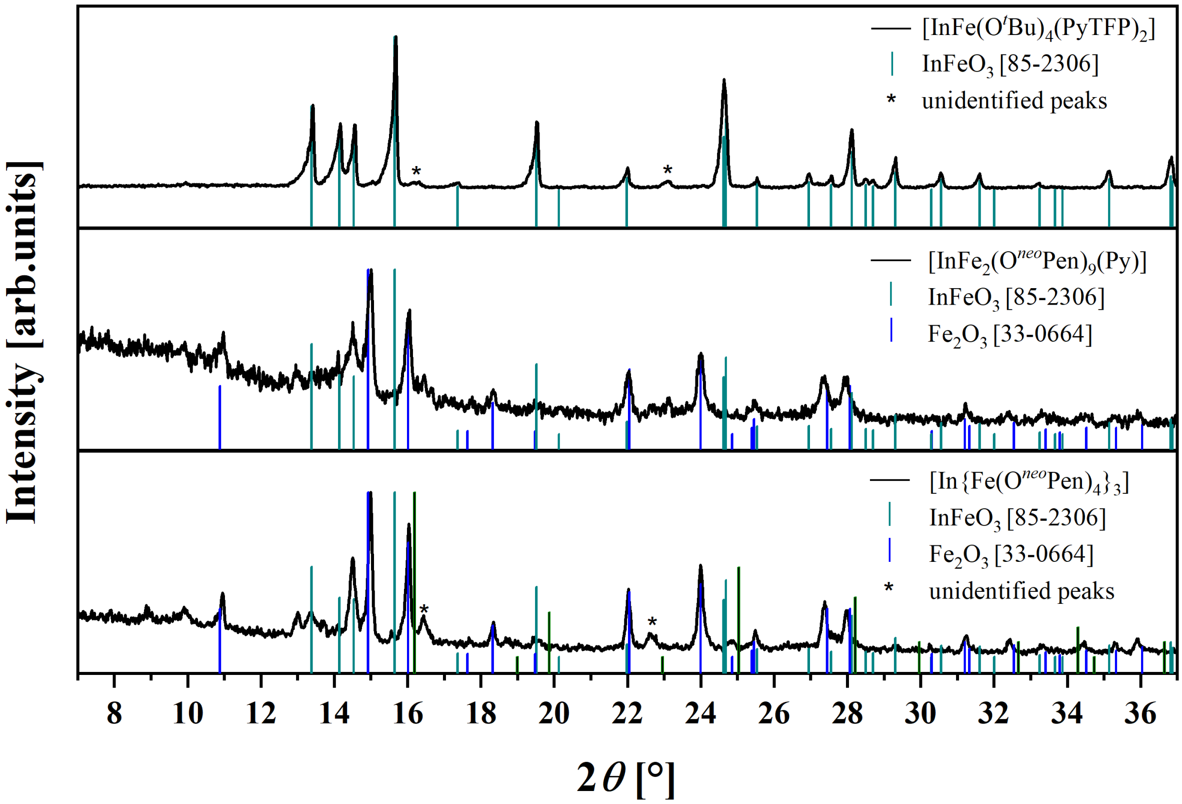

Figure 4: XRD plots of **1-3** after thermal decompositon at 1000 °C for 16 h with a heating rate of 300 °C/h.

The existence of crystalline phase as observed in the TEM data (Figure 5) and the identification of $InFeO_3$ as the crystalline phase (XRD analysis) suggested the preferential crystallization of $InFeO_3$ formed upon the decomposition of molecular precursor. Hence, it can be assumed that owing to chemically preorganized arrangement of the metal centers in **1**, its decomposition by heat treatment did not lead to segregation into iron and indium regions that ultimately would lead to the formation of iron and indium oxide phases. In contrast, only hexagonal $InFeO_3$ was observed in XRD (Figure 4), EDX and SAED measurements (Figure 5), that is a validation of the hypothesis that the initial chemical configuration present in the precursor molecule is maintained during the thermal treatment.

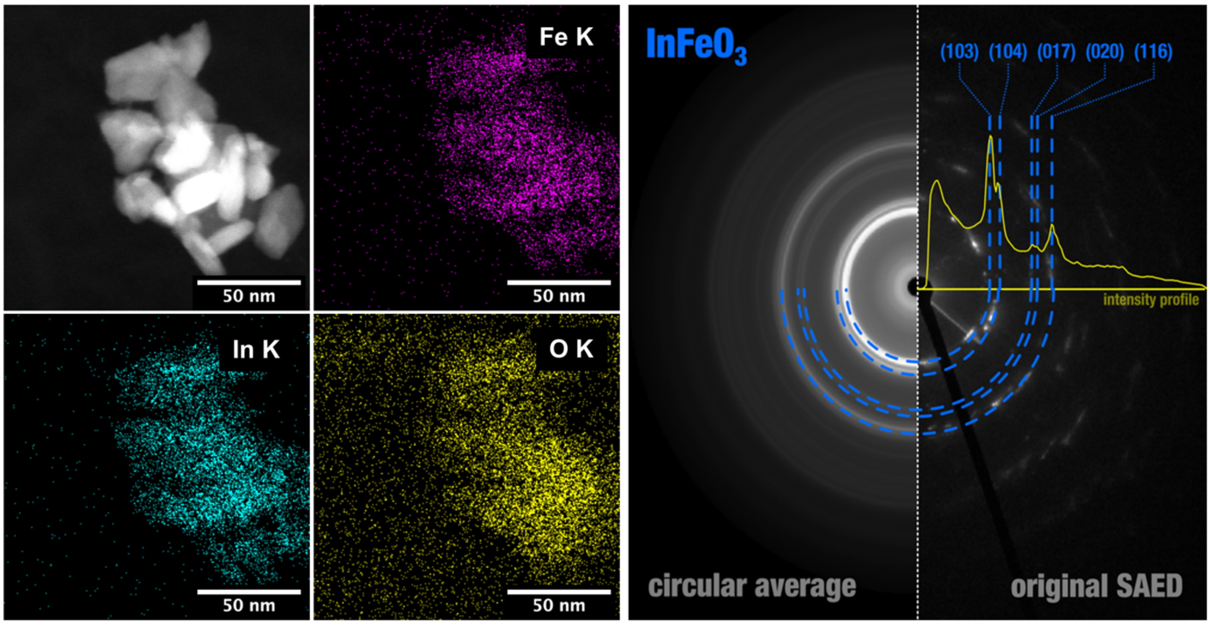

Figure 5: TEM images of 1 after thermal decompositon at 1000 °C with EDX mapping regarding indium (cyan), iron (magenta) and oxygen (yellow) as well as SAED pattern and circular averaged pattern with indexed $InFeO_3$ reflexes (blue for [85-2306]). The intensity profile (yellow) highlights all diffraction intensity of the circular averaged data.

TEM characterization of $InFeO_3/Fe_2O_3$ composites, synthesized by thermal decomposition of **2** and **3** at 1000 °C, showed agglomerated nanoparticles consisting of both $InFeO_3$ and Fe_2O_3 (Figure 6 and 7). A similar phase separation was observed in the decomposition of $[NdAl_3(OR)_{12}]$ that produced $NdAlO_3$ as the crystalline phase embedded in an amorphous alumina matrix.[5,65] The decomposition product of precursor **2** revealed a homogenous distribution of In, Fe and O (EDX, Figure 6) indicating the homogeneous formation of ternary $InFeO_3$ and Fe_2O_3 phases that was also observed in TEM images. In addition, the existence of both, $InFeO_3$ and Fe_2O_3, was verified by SAED study, represented in Figure 6.

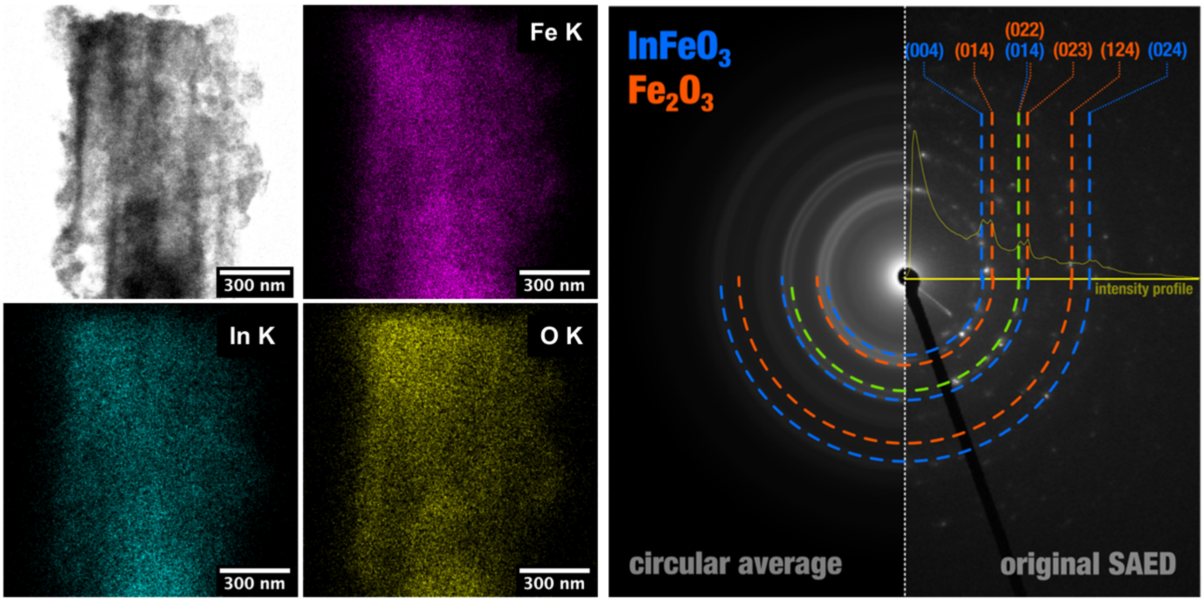

Figure 6: TEM images of **2** after thermal decompositon at 1000 °C with EDX mapping regarding indium (cyan), iron (magenta) and oxygen (yellow) as well as the SAED pattern and circular averaged pattern with indexed $InFeO_3$ (blue for [85-2306]) and Fe_2O_3 (orange for [33-0664]) reflexes. The intensity profile (yellow)highlights all diffraction intensity of the circular averaged data.

TEM images of the solid material obtained upon the decomposition of precursor **3** demonstrated different particle morphologies, when compared to the decomposition product of **2** (Figure 7). In some areas (e.g., spot 1) a lower concentration of indium, but a higher concentration iron is present, that represent the co-crystallization of $InFeO_3$ and α-Fe_2O_3 particles, which was also observed SAED measurement (Figure 7, right). Whereas in other spots (e.g., spot 2) a homogenous distribution if In, Fe and O exists, which indicates no formation of hematite in that area.

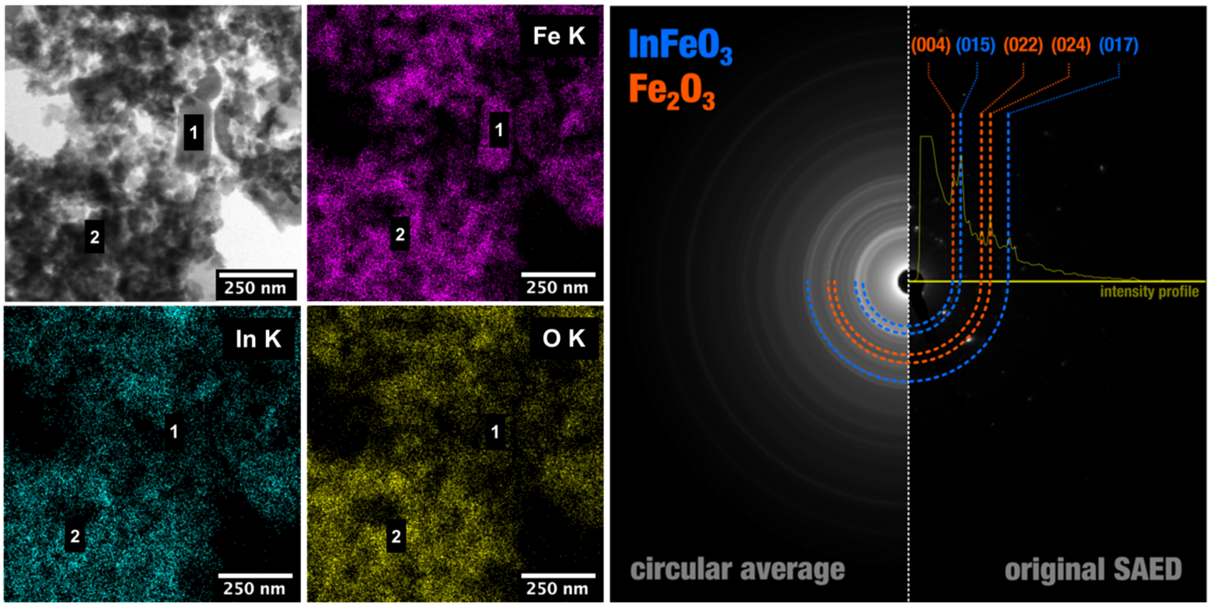

Figure 7: TEM images of **3** after thermal decompositon at 1000 °C with EDX mapping regarding indium (cyan), iron (magenta) and oxygen (yellow) as well as the SAED pattern and circular averaged pattern with indexed $InFeO_3$ (blue for [85-2306]) and Fe_2O_3 (orange for [33-0664]) reflexes. The intensity profile (yellow)highlights all diffraction intensity of the circular averaged data.

Further magnetic and spectroscopic analysis was done for the decomposition product of **1**, which did not show any hematite impurities in the XRD. The Moessbauer spectrum (Figure 8) showed characteristic absorption features of $InFeO_3$ with a strong doublet and additional weak sextet splitting that was confirmed by fitting parameters (Figure 8, table) that are in line with values reported for $InFeO_3$.[47,66]

doublet

	Isomer Shift δ (mm/s)	Quadrupole Splitting (mm/s)	Width (mm/s)
Reference	0.31	0.75	0.32
Sample	0.26	0.69	0.36

sextet

	Isomer Shift δ (mm/s)	Quadrupole Splitting (mm/s)	Width (mm/s)
Reference	0.37		49.3
Sample	0.45		50.7
Hematite	0.34	0.10	50.6

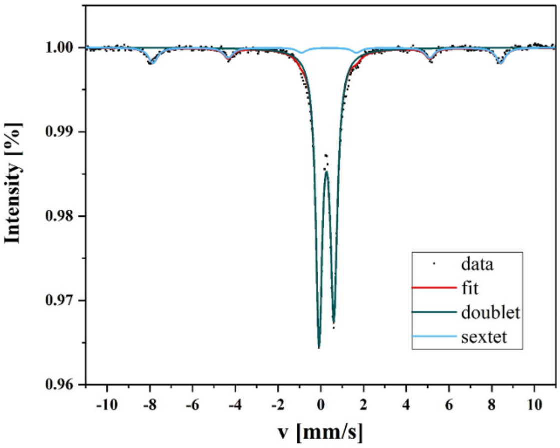

Figure 8: Moessbauer spectroscopy of decomposed **1** (black: sample, red: fit, green: doublet, blue: sextet) with values for isomer shift, quadrupole splitting and width for the sample as well as literature references.[47,67]

X-ray absorption spectroscopy performed at room temperature revealed the electronic structure of the material (Figure 9). The Fe-$L_{3,2}$ edge showed the distinct pre-edge feature at 707.1 eV of approximately half the intensity of the white line found for iron in the trivalent oxidation state in iron oxide (Figure 9, left).[68,69] Besides hematite, that was already excluded by XRD measurement, the existence of spinel phase couldn't be observed in the O-K edge, which showed no characteristic absorption features for hematite or maghemite in the pre-edge region compared to the reference spectrum (Figure 9, right). In contrast, the sample revealed absorption maxima at 530.8 eV, 531.1 eV, 534.6 eV and 538.1 eV, which are also known for hexagonal manganates ($RMnO_3$, with R=Y, Ln). These findings are in line with Moessbauer spectroscopy and XRD. However, the signals are broadened in contrast to spectra from a single crystalline hexagonal manganate.[70,71]

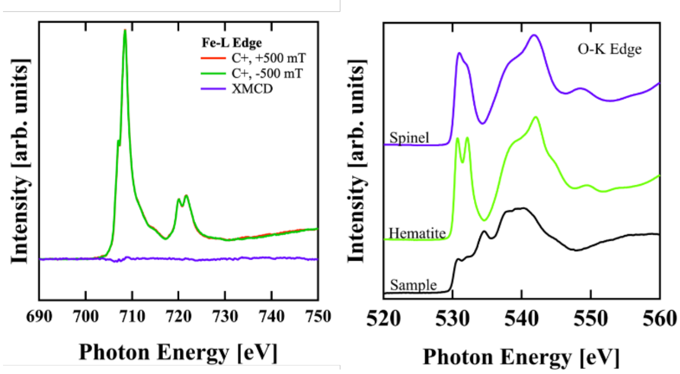

Figure 9: X-Ray absorption spectrum of **1**, left: Fe-$L_{2/3}$ edge, right: O-K edge with hematite and magnetite reference spectra.

Temperature (Figure 10a) and field-dependent (Figure 10b) magnetization measurements at lower temperatures of phase pure $InFeO_3$ powders revealed Curie-like paramagnetism and a signal around 160 K (Figure 10, left, red box) in the zero-field cooled (ZFC) curve with a drop-in magnetization during field cooled (FC) measurements, that indicates a first order magnetic phase transition. During cooling, the decrease in magnetization was seen at 175 K, while the very same phase transition was observed at 200 K during heating.

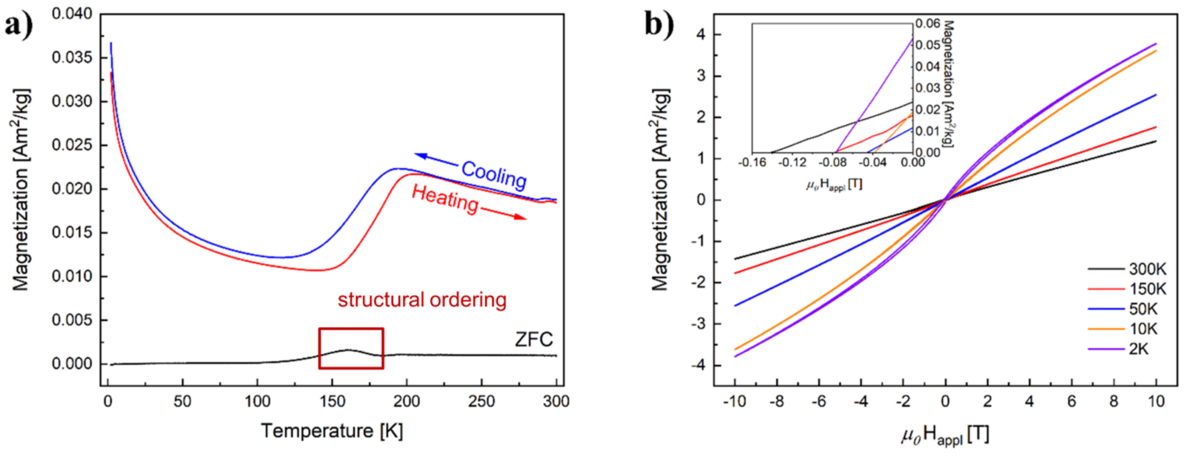

Figure 10: Field-cooled (FC, blue and red line) and zero-field cooled (ZFC) measurements (a) and magnetic hysteresis curves (b) at different temperatures of the $InFeO_3$ powder, obtained from **1**.

Field dependent magnetization measurements at temperatures ranging from 300 K to 2 K revealed a paramagnetic behavior at room temperature and the appearance of a hysteresis below 150 K, what was also described for epitaxially grown $InFeO_3$ on ZnO(001) *via* pulsed laser deposition.[72] Even though the magnetic anomaly in ZFC measurements was not observed for those films, the trend of spontaneous magnetization in ZFC measurements were reported for polycrystalline hexagonal ferrites and manganates with same symmetry.[73] In these reports, an increased exchange interaction between the Fe^{3+} atoms in the hexagonal is stated to cause the observed signal in the ZFC curve.[74]

CONCLUSION. Successful synthesis of heterometallic alkoxides ($[InFe(O^tBu)_4(PyTFP)_2]$ (**1**), $[InFe_2(O^{neo}Pen)_9(Py)]$ (**2**) and $[InFe_3(O^{neo}Pen)_{12}]$ (**3**)) allowed a molecular access to single-phase $InFeO_3$ (**1**) and $InFeO_3/Fe_2O_3$ nanocomposites (**2** and **3**). The cation stoichiometry in the precursors was deterministic for the formation of a ternary single-phase material and oxide-oxide nanocomposite originating from single-molecular sources. Thermal gravimetric studies in conjunction with powders X-ray diffractometry and electron microscopy provided an insight into the formation of chemically homogeneous precursors through the preorganized atomic arrangements and the thermodynamically induced phase formation (or separation) observed upon heat treatment. The preferred crystallization of the perovskite phase in the case of $InFeO_3/Fe_2O_3$ nanocomposites is probably due to the miscibility limits and favorable enthalpy of formation. Magnetic measurements of the material revealed a first order magnetic transition with an increase of the magnetization in the ZFC measurements that was explained by temperature induced reduction of the Fe-Fe distance and the corresponding increase in super-exchange. Recently, band gap calculations ($E_g = 2.5$ eV) and photoeletrochemical characterizations of $InFeO_3$, emphasized its water splitting potential by visible and ultraviolet light.[48]

EXPERIMENTAL SECTION

General Procedure

All syntheses were carried out under inert nitrogen gas atmosphere by using a *Stock* glass vacuum line. If not mentioned, all reagents were used without further purification. Used solvents were freshly distilled and dried over sodium. Suitable crystals for X-ray diffraction analysis were obtained by recrystallization in toluene at -18 °C for compounds **1**-**3**. The crystallographic data for all compounds is summarized in Table 1. The data collection for X-ray structure elucidation was performed on a STOE IPDS II diffractometer (Mo-Kα = 0.71073 Å, 50 kV, 30 mA) and the used programs for structure solution as well as the refinement are SIR-92[75], SHELXS[76], SHELXL[76] and WinGX[77,78]. Elemental analysis was performed using a HEKAtech CHNS Euro EA 3000 analyzer. TG analysis was performed by a TG/DSC1 (Mettler Toledo GmbH, Germany) apparatus using nitrogen gas and a heating rate of 10 °C/min. Powder X-Ray diffraction was measured on a STOE diffractometer with STADI MP system and either Mo-Kα ($\lambda = 0.71$ Å) or Cu-Kα radiation ($\lambda = 1.54$ Å). TEM characterizations with selected-area electron diffraction (SAED) as well as energy dispersive X-ray (EDX) studies of particle dispersions (toluene/*iso*-propylalcohol 1:1) were performed on a JEOL JEM-2200FS transmission electron microscope operated at an acceleration voltage of 200 kV. SAED analyses were performed using the software CrysTBox 1.10.[79] Moessbauer spectroscopy was measured on a Wissel spectrometer at ambient temperature. XAS measurements were carried out at the soft X-ray undulator beamline UE56/1-SGM at the synchrotron facility BESSY II in Berlin.

Table 1: Summary of crystallographic and refinement data for compounds **1-3**.

	1	**2**	**3**
formula	$InFeC_{32}H_{46}O_6N_2F_6$	$InFe_2C_{50}H_{104}O_9N$	$InFe_3C_{60}H_{132}O_{12}$
M [g mol^{-1}]	839.4	1089.9	1328.1
crystal system	triclinic	monoclinic	monoclinic
space group	$P\,\bar{1}$	$P\,2_1/c$	$P\,2/n$
a [Å]	8.90(8)	11.89(2)	11.35(7)
b [Å]	13.82(1)	42.86(6)	17.33(8)
c [Å]	16.44(1)	38.10(7)	19.96(1)
α [°]	88.1(6)	90	90
β [°]	81.6(6)	95.70(2)	102.18(5)
γ [°]	77.0(6)	90	90
V [Å^3]	1949.0(3)	19315.2(6)	3838.2(4)
Z	2	12	2
reflections collected	18866	32388	43190
independent reflections	8213	19944	6776
observed reflections	3771	1783	3495
goodness of fit	0.979	1.004	0.879
R(int)	0.111	0.093	0.200
R_1, wR_2 [$I>2\sigma(I)$]	0.089, 0.245	0.086, 0.231	0.061, 0.132
R_1, wR_2 (all data)	0.172, 0.285	0.121, 0.258	0.132, 0.163

Precursor Synthesis

[In{N(SiMe$_3$)$_2$}$_3$]: Bis(trimethylsilyl)amine (15.51 mL, 75 mmol) was cooled in liquid nitrogen and covered with a layer of *n*-BuLi (2.5 M in heptane, 30.00 mL, 75 mmol). After thawing, the mixture was slowly added to a solution of $InCl_3$ (5.50 g, 25 mmol) in dry THF (50 mL). The suspension was stirred for 3 h. Afterwards the solvent was removed under reduced pressure, and [Li{N(SiMe$_3$)}] was sublimated at 90 °C in vacuo (10^{-2} mbar) followed by sublimation of the crude product at 110 °C in vacuo (10^{-2} mbar). The resulting colorless solid was used for the next syntheses without further analysis, yield 12.24 g (22 mmol, 88%). Molar mass: 563.89 g mol^{-1}.

[Fe(O^{t}Bu)$_3$]$_2$: $FeCl_3$ (6.23 g, 38 mmol) in toluene (50 mL) was cooled in liquid nitrogen and THF (150 mL) was slowly added. The mixture was stirring while thawing. Afterwards a solution of KO^{t}Bu (12.8 g, 114 mmol) in THF (150 mL) was added. The mixture was stirred for 24 h at 80 °C and after that cooled down to room temperature. The solvent was removed under reduced pressure and the crude product was sublimated at 90 °C in vacuo (10^{-2} mbar), resulting in a green solid, yield 14.22 g (26 mmol, 68%). The product was used for the next step without further analysis. Molar mass: 550.38 g mol^{-1}; calcd: C 52.4, H 9.8; found C 51.2, H 9.9.

[InFe(O^{t}Bu)$_4$(PyTFP)$_2$] (1): [Fe(O^{t}Bu)$_3$]$_2$ (0.35 g, 0.63 mmol) was solved in toluene (6 mL) and one equivalent of PyTFP (0.12 g, 0.63 mmol) was added. Afterwards a solution of [In{N(SiMe$_3$)$_2$}$_3$] (0.71 g, 1.27 mmol) in toluene (6 mL) was added to the reaction mixture. The solution was stirred at 100 °C overnight and yellow crystals were obtained at -18 °C, that revealed the formation of **1**, yield 0.32 g (0.38 mmol, 61%). $C_{32}H_{46}FeInN_2O_6$ (839.4 g mol^{-1}): calcd: C 45.8, H 5.5, N 3.3; found C 46.9, H 6.4, N 3.5.

[InFe$_2$(O^{neo}Pen)$_9$(Py)] (2): For the preparation of [InFe$_2$(O^{neo}Pen)$_9$(Py)], [In{N(SiMe$_3$)$_2$}$_3$] (0.38 g, 0.64 mmol) in toluene (4 mL) was added to a solution of [Fe(O^{t}Bu)$_3$]$_2$ (0.33 g, 0.60 mmol) in toluene (6 mL). Afterwards pyridine (4 mL) and *neo*-pentanol (10 mL) were added. The orange solution was stirred over night at 60 °C and yellow crystals were obtained at -18°C, yield 0.55 g (0.51 mmol, 79%). $C_{50}H_{104}Fe_2InNO_9$ (1089.9 g mol^{-1}): calcd: C 55.1, H 9.6, N 1.3; found C 53.7, H 9.9, N 1.0.

[InFe$_3$(O^{neo}Pen)$_{12}$] (3): [InFe$_3$(O^{neo}Pen)$_{12}$] was synthesized by adding [In{N(SiMe$_3$)$_2$}$_3$] (0.12 g, 0.21 mmol) in Toluene (4 mL) to a solution of [Fe(O^{t}Bu)$_3$]$_2$ (0.17 g, 0.31 mmol) in toluene (6 mL), followed by the addition of *neo*-pentanol (10 mL). The mixture was stirred for

24 h at 60 °C yellow crystals were obtained at -18°C, yield 0.23 g (0.17 mmol, 83%). $InFe_3C_{60}H_{120}O_{12}$ (1328.1 g mol^{-1}): calcd: C 54.3, H 10.0; found C 55.6, H 10.2.

Material Synthesis

For material synthesis 100 mg of heterometallic indium iron precursors **1-3** were prepared under inert conditions, respectively and transferred in sealed flasks. The thermal decompositions of the green (**1**) and yellow (**2** and **3**) solids were performed in air at 1000 °C (16 h) with a heating rate of 300 °C/h.

ASSOCIATED CONTENT

Supporting Information

PDF-file of check cif CCDC 2045551, 2045554, 2045555 contain the supplementary crystallographic data for this paper. These data can be obtained free of charge via ww.ccdc.cam.ac.uk/data_request/cif,orby emailing data_request@ccdc.cam.ac.uk, or by contacting The Cambridge Crystallographic Data Centre, 12 Union Road, Cambridge CB2 1EZ, UK; fax: +44 1223 336033.

AUTHOR INFORMATION

Corresponding Author

*Sanjay Mathur - Institute of Inorganic Chemistry, University of Cologne; Greinstraße 6, D-50939 Cologne, Germany; Email: sanjay.mathur@uni-koeln.de

Author

Vanessa Nahrstedt - Institute of Inorganic Chemistry, University of Cologne; Greinstraße 6, D-50939 Cologne, Germany; Email: vnahrste@smail.uni-koeln.de

Daniel Stadler - Institute of Inorganic Chemistry, University of Cologne; Greinstraße 6, D-50939 Cologne, Germany; Email: daniel.stadler@uni-koeln.de

Thomas Fischer - Institute of Inorganic Chemistry, University of Cologne; Greinstraße 6, D-50939 Cologne, Germany; Email: t.fischer@uni-koeln.de

Tomas Duchoň - Peter Grünberg Institute (PGI-6), Research Centre Juelich GmbH, Leo-Brandt-Straße, D-52428 Juelich, Germany; Email: t.duchon@fz-juelich.de

David N. Müller - Peter Grünberg Institute (PGI-6), Research Centre Juelich GmbH, Leo-Brandt-Straße, D-52428 Juelich, Germany; Email: dav.mueller@fz-juelich.de

Claus M. Schneider - Peter Grünberg Institute (PGI-6), Research Centre Juelich GmbH, Leo-Brandt Straße, D-52428 Juelich, Germany; Email: c.m.schneider@fz-juelich.de

Notes

The authors declare no competing financial interest.

ACKNOWLEDGEMENT. This work was funded within the framework of the priority programme SPP1959 of the *Deutsche Forschungsgemeinschaft (DFG)*. Authors thank the University of Cologne and the Excellence Cluster "Quantum Matter and Materials" for the infrastructural support. We also acknowledge the support of Dr. Ingo Pantenburg as well as Ms. Silke Kremer (Core Facility X-ray Crystallography), Mr. Dirk Pullem (Elemental Analysis) and Mr. Fernando Maccari for magnetization measurements (TU Darmstadt, Germany). For Moessbauer spectroscopy we thank Dr. Dominika Zákutná (Charles University, Czech Republic). We thank HZB for the allocation of synchrotron radiation beamtime.

REFERENCES

(1) Mathur, S.; Veith, M.; Rapalaviciute, R.; Shen, H.; Goya, G. F.; Filho, W. L. M.; Berquo, T. S. Molecule Derived Synthesis of Nanocrystalline $YFeO_3$ and Investigations on Its Weak Ferromagnetic Behavior. *Chem. Mater.* **2004**, *16*, 1906–1913.

(2) Mathur, S.; Veith, M.; Ruegamer, T.; Hemmer, E.; Shen, H. Chemical Vapor Deposition of $MgAl_2O_4$ Thin Films Using Different Mg-Al Alkoxides: Role of Precursor Chemistry. *Chem. Mater.* **2004**, *16*, 1304–1312.

(3) Mathur, S.; Shen, H.; Lecerf, N.; Kjekshus, A.; Fjellvåg, H.; Goya, G. F. Nanocrystalline

Orthoferrite $GdFeO_3$ from a Novel Heterobimetallic Precursor. *Adv. Mater.* **2002**, *14*, 1405–1409.

(4) Bohr, C.; Yu, P.; Scigaj, M.; Hegemann, C.; Fischer, T.; Coll, M.; Mathur, S. Atomic Scale Growth of $GdFeO_3$ Perovskite Thin Films. *Thin Solid Films* **2020**, *698*, 137848(1)-137848(7).

(5) Mathur, S.; Veith, M.; Shen, H.; Hüfner, S.; Jilavi, M. H. Structural and Optical Properties of $NdAlO_3$ Nanocrystals Embedded in an Al_2O_3 Matrix. *Chem. Mater.* **2002**, *14*, 568–582.

(6) M. Veith; Mathur, S.; Lecerf, N.; Bartz, K.; Heintz, M.; Huch, V. Synthesis of $NdAlO_3/Al_2O_3$ Ceramic- Ceramic Composite by Single-Source Precursor CVD. *Chem. Mater.* **2000**, *12*, 271–274.

(7) Ojelere, O.; Graf, D.; Mathur, S. Molecularly Engineered Lithium-Chromium Alkoxide for Selective Synthesis of $LiCrO_2$ and Li_2CrO_4 Nanomaterials. *Inorganics* **2019**, *7*, 1–10.

(8) Jamil, A.; Schläfer, J.; Gönüllü, Y.; Lepcha, A.; Mathur, S. Precursor-Derived Rare Earth Metal Pyrochlores: $Nd_2Sn_2O_7$ Nanofibers and Thin Films As Efficient Photoabsorbers. *Cryst. Growth Des.* **2016**, *16*, 5260–5267.

(9) Mathur, S.; Cavelius, C.; Moh, K.; Shen, H.; Bauer, J. Cobalt Ferrite Nanoparticles from Single and Multi-Component Precursor Systems. *Z. Anorg. Allg. Chem.* **2009**, *635*, 898–902.

(10) Veith, M.; Haas, M.; Huch, V. Single Source Precursor Approach for the Sol-Gel Synthesis of Nanocrystalline $ZnFe_2O_4$ and Zinc - Iron Oxide Composites. *Chem. Mater.* **2005**, *17*, 95–101.

(11) Meyer, F.; Hempelmann, R.; Mathur, S.; Veith, M. Microemulsion Mediated Sol – Gel Synthesis of Nano-Scaled MAl_2O_4 (M = Co, Ni, Cu) Spinels from Single-Source Heterobimetallic Alkoxide Precursors. *J. Mater. Chem.* **1999**, *4*, 1755–1763.

(12) Mathur, S.; Cavelius, C.; Shen, H. $CoGa_2O_4$ Nanoparticles and Films Using a Single Molecular Source. *Z. Anorg. Allg. Chem.* **2009**, *635*, 2106–2111.

(13) Meyer, F.; Dierstein, A.; Beck, C.; Härtl, W.; Hempelmann, R.; Mathur, S.; Veith, M. Size-Controlled Synthesis of Nanoscaled Aluminum Spinels Using Heterobimetallic Alkoxide Precursors via Water/Oil Microemulsions. *Nanostructured Mater.* **1999**, *12*, 71–74.

(14) Kessler, V. G. Molecular Structure Design and Synthetic Approaches to the Heterometallic Alkoxide Complexes. *Chem. Commun.* **2003**, 1213–1222.

(15) Hubert-Pfalzgraf, L. G. Some Trends in the Design of Homo- and Heterometallic Molecular Precursors of High-Tech Oxides. *Inorg. Chem. Commun.* **2003**, *6*, 102–120.

(16) D. C. Bradley; Mehrotra, R. C.; Rothwell, I. P.; Singh, A. *Alkoxo and Aryloxo Derivatives of Metals*; Elsevier, **2001**.

(17) D. C. Bradley. Metal Alkoxides as Precursors for Electronic and Ceramic Materials. *Chem. Rev.* **1989**, *89*, 1317–1322.

(18) Li, X.; Zhang, B.; Ju, C.; Han, X.; Du, Y.; Xu, P. Morphology-Controlled Synthesis and Electromagnetic Properties of Porous Fe_3O_4 Nanostructures from Iron Alkoxide Precursors. *J. Phys. Chem. C* **2011**, *115*, 12350–12357.

(19) Gun’ko, Y. K.; Cristmann, U.; Kessler, V. G. Synthesis and Structure of the First FeII Heterometallic Alkoxide $[(\mathrm{THF})\mathrm{NaFe}(\mathrm{O}^{t}\mathrm{Bu})_3]_2$ − a Possible Precursor for New Materials. *Eur. J. Inorg. Chem.* **2002**, 1029–1031.

(20) Mishra, S.; Daniele, S. Molecular Engineering of Metal Alkoxides for Solution Phase Synthesis of High-Tech Metal Oxide Nanomaterials. *Chem. - A Eur. J.* **2020**, *26*, 9292–

(21) Gschwind, F.; Crochet, A.; Maudez, W.; Fromm, K. M. From Alkaline Earth Ion Aggregates via Transition Metal Coordination Polymer Networks towards Heterometallic Single Source Precursors for Oxidic Materials. *Chimia* **2010**, *64*, 299–

(22) Herrig, H.; Hempelmann, R. Microemulsion Mediated Synthesis of Ternary and

Quaternary Nanoscale Mixed Oxide Ceramic Powders. *Nanostructured Mater.* **1997**, *9*, 241–244.

(23) Boyle, T. J.; Sears, J. M.; Perales, D.; Cramer, R. E.; Lu, P.; Chan, R. O.; Hernandez-Sanchez, B. A. Synthesis and Characterization of Tris(Trimethylsilyl)Siloxide Derivatives of Early Transition Metal Alkoxides That Thermally Convert to Varied Ceramic-Silica Architecture Materials. *Inorg. Chem.* **2018**, *57*, 8806–8820.

(24) Lu, H.; Wright, D. S.; Pike, S. D. The Use of Mixed-Metal Single Source Precursors for the Synthesis of Complex Metal Oxides. *Chem. Commun.* **2020**, *56*, 854–871.

(25) Schläfer, J.; Stucky, S.; Tyrra, W.; Mathur, S. Heterobi- and Trimetallic Cerium(IV) Tert -Butoxides with Mono-, Di-, and Trivalent Metals (M = K(I), Ge(II), Sn(II), Pb(II), Al(III), Fe(III)). *Inorg. Chem.* **2013**, *52*, 4002–4010.

(26) Veith, M.; Grätz, F.; Huch, V. $Fe_9O_3(OC_2H_5)_{21}\cdot C_2H_5OH$ - A New Structure Type of an Uncharged Iron(III) Oxide Alkoxide Cluster. *Eur. J. Inorg. Chem.* **2001**, 367–368.

(27) Veith, M.; Hill, S.; Huch, V. Synthese Und Charakterisierung von In^{III}-Sn^{II}-Halogenido-Alkoxiden und von Indiumtri-*tert*-butoxid. *Z. Anorg. Allg. Chem.* **2001**, *627*, 1495–1504.

(28) Spandl, J.; Kusserow, M.; Brüdgam, I. Alkoxo-Verbindungen Des Dreiwertigen Eisen: Synthese Und Charakterisierung von $[Fe_2(OtBu)_6]$, $[Fe_2Cl_2(OtBu)_4]$, $[Fe_2Cl_4(OtBu)_2]$ und $[N(NBu)_4]_2[Fe_6OCl_6(OMe)_{12}]$. *Z. Anorg. Allg. Chem.* **2003**, *629*, 968–974.

(29) Kusserow, M.; Spandl, J. Alkoholyse von $[Fe_2(O^tBu)_6]$ als einfacher Weg zu neuen Eisen(III)-Alkoxo-Verbindungen: Synthesen und Kristallstrukturen von $[Fe_2(OtAmyl)_6]$, $[Fe_5OCl(OiPr)_{12}]$, *Z. Anorg. Allg. Chem.* **2006**, *632*, 885–892.

(30) Schläfer, J.; Tyrra, W.; Mathur, S. Erratum: Octakis(*tert*-butoxo)dicerium(IV) $[Ce_2(O^tBu)_8]$: Synthesis, Characterization, Decomposition, and Reactivity, *Inorg. Chem.* **2014**, *53*, 2751–2753.

(31) Veith, M.; Mathur, S.; Shen, H.; Lecerf, N.; Hu, S.; Jilavi, M. H. Single-Step Preparation of Oxide - Oxide Nanocomposites : Chemical Vapor Synthesis of $LnAlO_3/Al_2O_3$ (Ln=Pr,

Nd) Thin Films. *Chem. Mater.* **2001**, *3*, 4041–4052.

(32) Appel, L.; Fiz, R.; Tyrra, W.; Pantenburg, I.; Mathur, S. Design of Volatile Mixed-Ligand Tantalum(V) Compounds as Precursors to Ta_2O_5 Films. *Cryst. Growth Des.* **2015**, *15*, 1141–1149.

(33) Graf, D.; Schläfer, J.; Garbe, S.; Klein, A.; Mathur, S. Interdependence of Structure, Morphology, and Phase Transitions in CVD Grown VO_2 and V_2O_3 Nanostructures. *Chem. Mater.* **2017**, *29*, 5877–5885.

(34) Lepcha, A.; Appel, L.; Frank, M.; Mathur, S.; Graf, D.; Queralt, A. Electrospun $SrNb_2O_6$ Photoanodes from Single-Source Precursors for Photoelectrochemical Water Splitting. *Sol. Energy Mater. Sol. Cells* **2020**, *210*, 110485(1)-110485(6).

(35) Straub, M. D.; Leduc, J.; Frank, M.; Raauf, A.; Lohrey, T. D.; Minasian, S. G.; Mathur, S.; Arnold, J. Chemical Vapor Deposition of Phase-Pure Uranium Dioxide Thin Films from Uranium(IV) Amidate Precursors. *Angew. Chem. - Int. Ed.* **2019**, *58*, 5749–5753.

(36) Wijk, M.; Norrestam, R.; Nygren, M.; Westin, G. Synthesis, Characterization, and Structural Determination of the Bimetallic Alkoxide $ErAl_3(OC_3H_7{}^i)_{12.}$, *Inorg. Chem.* **1996**, *35*, 1077–1079.

(37) Westin, G. Synthesis and Properties of Erbium Isopropoxides: Structural Characterization of $Er_5O(OPr^i)_{13}$. *J. Solid State Chem.* **1998**, *141*, 168–176.

(38) Kritikos, M.; Wijk, M.; Westin, G. $[Er_2Al_2(O^iPr)_{12}(HO^iPr)_2]$, a Novel Heterobimetallic Alkoxide. *Acta Crystallogr. Sect. C Cryst. Struct. Commun.* **1998**, *54*, 576–578.

(39) Moustiakimov, M.; Kritikos, M.; Westin, G. $Nd[Al(^iPrO)_4]_3$, a Novel Tetranuclear Alkoxide Forming Merohedrally Twinned Crystals. *Acta Crystallogr. Sect. C Cryst. Struct. Commun.* **2001**, *57*, 515–516.

(40) Berger, E.; Westin, G. Structure of a Hepta-Nuclear Termetallic Oxo-Alkoxide: $Eu_3K_3TiO_2(OBu^t)_{11}(OMe/OH)(HOBu^t)$. *J. Sol-Gel Sci. Technol.* **2010**, *53*, 681–688.

(41) Sharma, M. K.; Sharma, M.; Singh, A.; Mehrotra, R. C. Synthesis and Characterization

of Heterobimetallic Isopropoxides of Bismuth (III). *Indian J. Chem. - Sect. A Inorganic, Phys. Theor. Anal. Chem.* **2001**, *40*, 1226–1228.

(42) Mishra, S.; Agarwal, R.; Singh, A. Four Novel Classes of Heterobimetallic Isopropoxides of Chromium(III). *Transit. Met. Chem.* **2002**, *27*, 712–715.

(43) Mathur, S.; Shen, H.; Rapalaviciute, R.; Donia, N. Kinetically Controlled Synthesis of Metastable $YAlO_3$ through Molecular Level Design. *J. Mater. Chem.* **2004**, *14*, 3259–3265.

(44) Hemmer, E.; Huch, V.; Adlung, M.; Wickleder, C.; Mathur, S. Homo- and Heterometallic Terbium Alkoxides - Synthesis, Characterization and Conversion to Luminescent Oxide Nanostructures. *Eur. J. Inorg. Chem.* **2011**, 2148–2157.

(45) Veith, M.; Mathur, S.; Huch, V. Designed Synthesis and Molecular Structure of the First Heterotermetallic Alkoxide. *J. Am. Chem. Soc.* **1996**, *118*, 903–904.

(46) Giaquinta, D. M.; Davis, W. M.; zur Loye, H. C. Structure of Indium Iron Oxide. *Acta Crystallogr. Sect. C Cryst. Struct. Commun.* **1994**, *50*, 5–7.

(47) Downie, L. J.; Goff, R. J.; Kockelmann, W.; Forder, S.; Parker, J. E.; Morrison, F. D.; Lightfoot, P. Structural, Magnetic and Electrical Properties of the Hexagonal Ferrites $MFeO_3$ (M=Y, Yb, In). *J. Solid State Chem.* **2012**, *190*, 52–60.

(48) Zhang, B.; Seki, M.; Zhou, H.; Chen, J.; Tabata, H. $InFeO_3$ Photoelectrode with Two-Dimensional Superlattice for Visible- and Ultraviolet-Light-Driven Water Splitting. *APL Mater.* **2020**, *8*, 6–11.

(49) Fujita, K.; Kawamoto, T.; Yamada, I.; Hernandez, O.; Hayashi, N.; Akamatsu, H.; Lafargue-Dit-Hauret, W.; Rocquefelte, X.; Fukuzumi, M.; Manuel, P.; Studer, A. J.; Knee, C. S.; Tanaka, K. $LiNbO_3$-Type $InFeO_3$: Room-Temperature Polar Magnet without Second-Order Jahn-Teller Active Ions. *Chem. Mater.* **2016**, *28*, 6644–6655.

(50) Lima, A. F.; Lalic, M. V. Comparative Study of Magnetic and Electronic Properties of Room-Temperature Polar Magnets $ScFeO_3$ and $InFeO_3$. *Int. J. Quantum Chem.* **2019**,

119, 1–8.

(51) Liu, S.; Wang, R.; Wang, C.; Wang, F.; Xu, Y.; Sun, K.; Hao, X. Asymmetric Covalence Bonding between In 5s and O 2p States in Ferroelectric $InFeO_3$. *J. Phys. Chem. Solids* **2018**, *122*, 1–7.

(52) Ikeda, N.; Ohsumi, H.; Ohwada, K.; Ishii, K.; Inami, T.; Kakurai, K.; Murakami, Y.; Yoshii, K.; Mori, S.; Horibe, Y.; Kitô, H. Ferroelectricity from Iron Valence Ordering in the Charge-Frustrated System $LuFe_2O_4$. *Nature* **2005**, *436*, 1136–1138.

(53) Oka, K.; Azuma, M.; Hayashi, N.; Muranaka, S.; Narumi, Y.; Kindo, K.; Ayukawa, S.; Kato, M.; Koike, Y.; Shimakawa, Y.; Takano, M. Charge and Magnetic Orderings in the Triangular-Lattice Antiferromagnet $InFe_2O_4$. *J. Phys. Soc. Japan* **2008**, *77*, 2–6.

(54) Akaiwa, K.; Kaneko, K.; Fujita, S.; Chikoidze, E.; Dumont, Y. Room Temperature Ferromagnetism in Conducting α-$(In_{1-X}Fe_x)_2O_3$ Alloy Films. *Appl. Phys. Lett.* **2015**, *106*, 1–5.

(55) D., S. R.; Vincent, H.; Kjekshus, A.; Rakke, T.; Allen, G. C.; Warren, K. D. *Chemical Bonding in Solids*; Springer-Verlag: Berlin Heidelberg, **1974**.

(56) Appel, L.; Fiz, R.; Tyrra, W.; Mathur, S. New Iso-Propoxides, Tert-Butoxides and Neo-Pentoxides of Niobium(v): Synthesis, Structure, Characterization and Stabilization by Trifluoroheteroarylalkenolates and Pyridine Ligands. *Dalt. Trans.* **2012**, *41*, 1981–1990.

(57) Leduc, J.; Ravithas, R.; Rathgeber, L.; Mathur, S. New Air-Stable Uranium(IV) Complexes with Enhanced Volatility. *New J. Chem.* **2015**, *39*, 7571–7574.

(58) Brückmann, L.; Tyrra, W.; Stucky, S.; Mathur, S. Novel Air-Stable and Volatile Bis(Pyridylalkenolato)Palladium(II) and -Platinum(II) Derivatives. *Inorg. Chem.* **2012**, *51*, 536–542.

(59) Heidemann, T.; Mathur, S. Air-Stable and Volatile Bis(Pyridylalkenolato)Germanium(II), -Tin(II), and -Lead(II) Complexes. *Eur. J. Inorg. Chem.* **2014**, 506–510.

(60) Fornalczyk, G.; Valldor, M.; Mathur, S. Monomeric Iron Heteroarylalkenolates: Structural Design Concepts and Investigations on Their Application in Chemical Vapor Deposition. *Cryst. Growth Des.* **2014**, *14*, 1811–1818.

(61) Büyükyazi, M.; Hegemann, C.; Lehnen, T.; Tyrra, W.; Mathur, S. Molecular Co(II) and Co(III) Heteroarylalkenolates as Efficient Precursors for Chemical Vapor Deposition of Co3O4 Nanowires. *Inorg. Chem.* **2014**, *53*, 10928–10936.

(62) Schläfer, J.; Graf, D.; Fornalczyk, G.; Mettenbörger, A.; Mathur, S. Fluorinated Cerium(IV) Enaminolates: Alternative Precursors for Chemical Vapor Deposition of CeO2 Thin Films. *Inorg. Chem.* **2016**, *55*, 5422–5429.

(63) Appel, L.; Leduc, J.; Webster, C. L.; Ziller, J. W.; Evans, W. J.; Mathur, S. Synthesis of Air-Stable, Volatile Uranium(IV) and (VI) Compounds and Their Gas-Phase Conversion to Uranium Oxide Films. *Angew. Chem. - Int. Ed.* **2015**, *54*, 2209–2213.

(64) Giebelhaus, I.; Müller, R.; Tyrra, W.; Pantenburg, I.; Fischer, T.; Mathur, S. First Air Stable Tin(II) β-Heteroarylalkenolate: Synthesis, Characterization and Application in Chemical Vapor Deposition. *Inorganica Chim. Acta* **2011**, *372*, 340–346.

(65) Leduc, J.; Goenuellue, Y.; Ghamgosar, P.; You, S.; Mouzon, J.; Choi, H.; Vomiero, A.; Grosch, M.; Mathur, S. Electronically-Coupled Phase Boundaries in α-Fe_2O_3/Fe_3O_4 Nanocomposite Photoanodes for Enhanced Water Oxidation. *ACS Appl. Nano Mater.* **2019**, *2* , 334–342.

(66) Nodari, I.; Alebouyeh, A.; Brice, J. F.; Gerardin, R.; Evrard, O. Caracterisation de Nouveau Ferrites d'indium: $In_2Fe_4O_9$ et $InFeO_3$. *Mat. Res. Bull.* **1988**, *23*, 1039–1044.

(67) Machala, L.; Zboril, R.; Gedanken, A. Amorphous Iron(III) Oxide - A Review. *J. Phys. Chem. B* **2007**, *111*, 4003–4018.

(68) Fischer, T.; Stadler, D.; Mueller, D. N.; Brede, T.; Sarkar, A.; Giesen, M.; Schneider, C. M.; Volkert, C. A.; Mathur, S. Magnetic Field-Assisted Chemical Vapor Deposition of Iron Oxide Thin Films: Influence of Field − Matter Interactions on Phase Composition

and Morphology. *J. Phys. Chem. Lett.* **2019**, *10*, 6253–6259.

(69) Kim, D. H.; Lee, H. J.; Kim, G.; Koo, Y. S.; Jung, J. H.; Shin, H. J.; Kim, J. Y.; Kang, J. S. Interface Electronic Structures of $BaTiO_3$ @X Nanoparticles (X=γ-Fe_2O_3, Fe_3O_4, α-Fe_2O_3, and Fe) Investigated by XAS and XMCD. *Phys. Rev. B - Condens. Matter Mater. Phys.* **2009**, *79*, 2–5.

(70) Cho, D. Y.; Kim, J. Y.; Park, B. G.; Rho, K. J.; Park, J. H.; Noh, H. J.; Kim, B. J.; Oh, S. J.; Park, H. M.; Ahn, J. S.; Ishibashi, H.; Cheong, S. W.; Lee, J. H.; Murugavel, P.; Noh, T. W.; Tanaka, A.; Jo, T. Ferroelectricity Driven by y D0-Ness with Rehybridization in $YMnO_3$. *Phys. Rev. Lett.* **2007**, *98*, 1–4.

(71) Asokan, K.; Dong, C. L.; Bao, C. W.; Tsai, H. M.; Chiou, J. W.; Chang, C. L.; Pong, W. F.; Duran, P.; Moure, C.; Peña, O. Comparison of Electronic Structures of Orthorhombic and Hexagonal Manganites Studied by X-Ray Absorption Spectroscopy. *Solid State Commun.* **2005**, *134*, 821–826.

(72) Seki, M.; Konya, T.; Inaba, K.; Tabata, H. Epitaxial Thin Films of $InFe_2O_4$ and $InFeO_3$ with Two-Dimensional Triangular Lattice Structures Grown by Pulsed Laser Deposition. *Appl. Phys. Express* **2010**, *3*, 5–8.

(73) Yamamoto, N.; Takagi, H.; Katsufuji, T.; Masaki, M.; Mori, S.; Moritomo, Y. Dielectric and Magnetic Anomalies and Spin Frustration in Hexagonal $RMnO_3$ (R=Y, Yb, and Lu). *Phys. Rev. B - Condens. Matter Mater. Phys.* **2001**, *64*, 1–6.

(74) Masuno, A.; Ishimoto, A.; Moriyoshi, C.; Hayashi, N.; Kawaji, H.; Kuroiwa, Y.; Inoue, H. Weak Ferromagnetic Transition with a Dielectric Anomaly in Hexagonal $Lu_{0.5}Sc_{0.5}FeO_3$. *Inorg. Chem.* **2013**, *52*, 11889–11894.

(75) Altomare, A.; Cascarano, G.; Giacovazzo, C.; Guagliardi, A. Istituto Di Ricerca per Io Sviluppo Di. *J. Appl. Cryst.* **1994**, *27*, 435–435.

(76) Sheldrick, G. M. A Short History of SHELX. *Acta Cryst.* **2008**, *A64*, 112–122.

(77) Farrugia, L. J. WinGX Suite for Small- Molecule Single-Crystal Crystallography

DISCUS , a Program for Diffuse Scattering and Defect Structure Simulations ± Update PowderX : Windows-95-Based Program for Powder X-Ray Diffraction Data Processing. *J. Appl. Cryst.* **1999**, *32*, 837–838.

(78) Farrugia, L. J. WinGX and ORTEP for Windows : An Update. *J. Appl. Cryst.* **2012**, *45*, 849–854.

(79) Klingel, M. More Features, more tools, more CrysTBox. *J. Appl. Cryst.* **2017**, *50,* 1226-1234.

SYNOPSIS. Heterometallic mixed-metal alkoxides based on indium and iron, possessing diverse In:Fe stoichiometry and different structural motifs, were synthesized and structurally characterized ([InFe(O^{t}Bu)$_4$(PyTFP)$_2$] (**1**), [InFe$_2$(O^{neo}Pen)$_9$(Py)] (**2**), [InFe$_3$(O^{neo}Pen)$_{12}$] (**3**)). Thermal decomposition of **1-3** under ambient conditions generated ternary oxide InFeO$_3$ with additional Fe$_2$O$_3$ present as a secondary for **2** and **3**, which is programmed in the stoichiometric composition of the precursors. The intimate mixing of different phases in the nanocomposites was confirmed by transmission electron microscopy.